



Mid- and long-wave infrared point spectrometer (MLPS): a miniature space-borne science instrument

XIANGWEN CHEN,¹ MATTHEW E. KENYON,^{1,*}
WILLIAM R. JOHNSON,¹ JORDANA BLACKSBERG,¹
DANIEL W. WILSON,¹ CAROL A. RAYMOND,¹
AND BETHANY L. EHLMANN^{1,2} 

¹Jet Propulsion Laboratory, California Institute of Technology, Pasadena, CA 91109, USA

²Division of Geological and Planetary Sciences, California Institute of Technology, Pasadena, CA 91125, USA

*mkenyon@jpl.nasa.gov

Abstract: The mid- and long-wave infrared point spectrometer (MLPS) is an infrared point spectrometer that utilizes unique technologies to meet the spectral coverage, spectral sampling, and field-of-view (FOV) requirements of many future space-borne missions in a small volume with modest power consumption. MLPS simultaneously acquires high resolution mid-wave infrared ($\sim 2\text{--}4\ \mu\text{m}$) and long-wave infrared ($\sim 5.5\text{--}11\ \mu\text{m}$) measurements from a single, integrated instrument. The broadband response of MLPS can measure spectroscopically resolved reflected and thermally emitted radiation from a wide range of targets and return compositional, mineralogic, and thermophysical science from a single data set. We have built a prototype MLPS and performed end-to-end testing under vacuum showing that the measured spectral response and the signal-to-noise ratio (SNR) for both the mid-wave infrared (MIR) and long-wave infrared (LIR) channels of MLPS agree with established instrument models.

© 2022 Optica Publishing Group under the terms of the [Optica Open Access Publishing Agreement](#)

1. Introduction

Highly capable imaging and point spectrometers have been demonstrated recently on the Dawn [1], Hayabusa2 [2], and OSIRIS-REx [3] missions to asteroids. However, on most current missions, separate instruments are used to measure the reflected and thermally emitted radiation from small bodies. Moreover, these instruments are typically large and are not compatible with the emerging classes of small satellites and small landers. The mini-neutron spectrometer developed for the LunaH-Map CubeSat [4]) can quantify H abundance coarsely for a slow flyby, but precise estimates require weeks to months of integration, preferably from orbit, making volatile heterogeneity assessment for flyby missions difficult to impossible with this technique. In contrast, a point spectrometer with integrated wavelength range coverage in the infrared is both feasible for miniaturization and scientifically compelling for science related to volatiles and rock/regolith composition.

The mid- and long-wave infrared point spectrometer (MLPS) was initially conceived as a miniaturized ($\sim 2\text{U}$) payload for single- or multi-spacecraft CubeSat/SmallSat missions to provide quantitative data to answer three specific questions relevant to how small bodies (asteroids, Martian moons, comets, etc.) formed and what information they reveal about the dynamical evolution of the solar system: (1) What is the quantity of water in each object? (2) In what phase(s) is the water incorporated (e.g., ice vs. hydrated silicate minerals)? and (3) Are organics or other volatiles present, and if so, what types and in what form? Similar high priority science questions answerable with data from the MIR and LIR turn up in the science and exploration of planetary surfaces across the solar system from terrestrial bodies to icy worlds. With the

growing number of small satellite (e.g., SIMPLEX [5]) and small lander (e.g., CLPS, PRISM [6]) opportunities, MLPS' compact design and science performance have come to the forefront as a highly relevant instrument for both small satellite and mass-constrained landed mission implementations.

Here we demonstrate the system-level design and performance of MLPS, maturing it to a state-of-readiness for future flight proposals, i.e., TRL-6 according to NASA technology readiness levels. Though MLPS specifications (e.g., wavelength range, field-of-view) can be tuned to fit a wide range of applications, in this work we have focused MLPS performance requirements and demonstrated its capabilities on a baseline design built around three scientific goals (Table 1):

Table 1. MLPS' driving requirements are set to achieve 3 scientific goals, relevant to exploring planetary surfaces across the solar system

Goals	Example Objectives	MLPS Driving Measurement Requirements
Volatiles: Understand form, quantity, distribution, temporal variability, and resource potential of water, organics, and other volatiles	Determine form and concentration of OH and H ₂ O in rocks and regolith	Spectral range encompassing OH, bound H ₂ O, H ₂ O ice absorptions and emissivity maxima (2.7–3.0; 5.5–7.0 μm) Spectral resolution <15 nm MIR, <400 nm LIR SNR >50 (surface temperature >~250 K)
	Detect ammonia and aliphatic organic matter	Spectral range encompassing N-H absorptions of ammonium at 3.1 μm, C-H absorptions at 3.4 μm
Geology: Understand Igneous Processes, Stratigraphy, Evolution of Surfaces	Map spatial relationships between compositionally distinct materials	Multiple measurement points at <3 mrad IFOV spot size
	Determine the composition of rocks and soils by identification of key lithologies and minerals	Christiansen Feature of Si-O emissivity (7–11 μm) to discriminate silicate lithologies <300 nm spectral resolution in LIR
Thermophysical/ Geotechnical: Understand temperature variation, grain size, and porosity	Determine the grain size, packing, and thermophysical properties of the planetary surface	Measure surface temperatures 90–400 K
		Measure transparency features from 5.5–10 μm that can provide grain size.

Goal 1: Determine the form, abundance, distribution, and time variation of volatiles. MLPS' wavelength range, spectral resolution, and signal-to-noise ratio (SNR) in the 2–4 μm range are optimized to discriminate the form and quantity of water at the surface – OH, adsorbed H₂O, or H₂O ice – via measurement of the OH/H₂O stretch vibration at ~3 μm (Fig. 1(a)). A spectral resolution of ≤15 nm, distinguishes water ice from OH in minerals and most forms of adsorbed H₂O [7]. With sufficient integration time on a sunlit surface, MLPS can also sense the H₂O bend at ~6 μm in its 5.5–11 μm channels (Fig. 1(b)). Additional volatiles like C-H in aliphatic organics, NH₄⁺ in minerals, and NH₃, CO₂, H₂S and CH₄ ices also have diagnostic absorptions in MLPS' 2–4 μm spectral range as well as in the longer wavelength range. The dual wavelength range measures volatile content and temperature simultaneously for surfaces and thereby enables accurate quantification by correction of the thermal emission addition to the OH/H₂O 3-μm feature, particularly important for bodies with surface temperatures >~250 K, and understanding temperature controls on volatile distribution. Applications include mapping the compositional heterogeneity of water-rich asteroids [8], quantification of water on airless bodies like the Moon [9], and investigation of ice-organic mixtures in bodies of the outer solar system [10].

Goal 2: Determine the composition of rocks and soils and study the stratigraphy and the evolution of the planetary surfaces. The MLPS LIR wavelength range captures the Si-O feature (7–11 μm) related to silicate polymerization and can thus resolve the presence of key minerals, identify discrete silicate lithologies, and distinguish amorphous versus crystalline materials. MLPS is optimized to measure changes in the position of the Christiansen feature, the

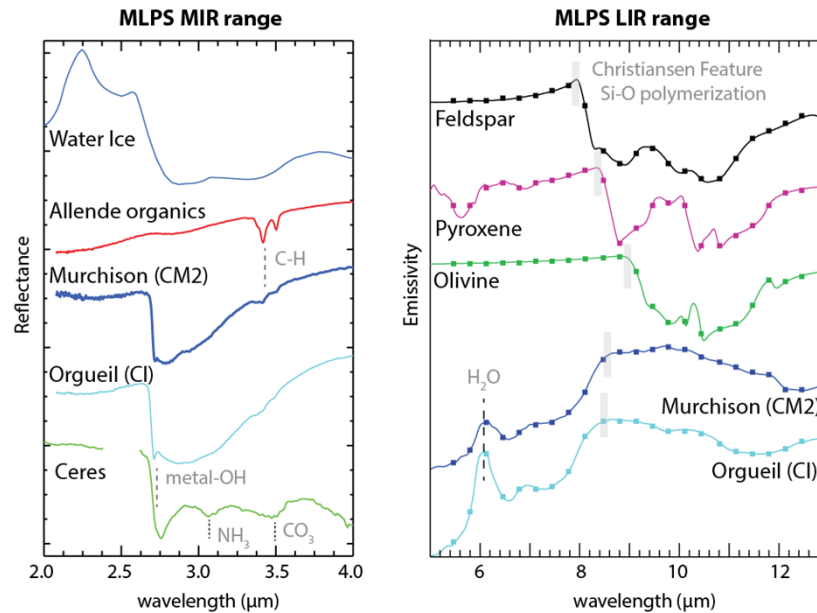


Fig. 1. Spectra of key materials in regions covered by MLPS. MLPS has 200 and 22 (boxes, right) channels covering the ranges between 2–4 and 5.5–11 μm , respectively. Spectra are from the Salisbury spectral library except for Ceres from De Sanctis et al. [14].

shortwave emissivity maximum of the Si-O stretch, which varies from 7–9 μm from quartz to feldspar to pyroxene to olivine, i.e. with silica polymerization (Fig. 1(b)). The assemblage of igneous minerals or hydrous silicates and their crystallinity can thus be determined to enable quantitative modeling of surface composition and, tracing the history of interior, volcanic, and impact processes affecting a planetary surface. Examples include mapping the degree of silicate alteration in asteroids [11], compositional discrimination of igneous units on the Moon [12], and mapping stratigraphic variation on Mars [13].

Goal 3: Determine the thermophysical and geotechnical planetary surface properties. Multiple time-of-day measurements in the MIR and LIR spectral ranges provide detailed measurements of diurnal temperature range to determine surface thermal inertia, affected by rock abundance, particle size, and porosity. LIR data in the transparency feature region (5.5–8 μm) also allow independent estimation of grain size for particulate surfaces.

Collectively, in addition to their relevance for planetary science, these capabilities also provide information relevant to human exploration and planetary defense. MLPS enables assessment of the quantity and extractability of resources from water-rich targets for In Situ Resource Utilization (ISRU) as well as generates geotechnical data for interaction with planetary surfaces and for studies of asteroid thermophysical properties.

2. MLPS design

To achieve the science requirements in Table 1, we designed MLPS to be a compact ($\sim 2\text{U}$), high performance spectrometer covering both the MIR (2–4 μm) and LIR (5.5–11 μm). While many spectrometers with a diversity of performance characteristics exist, we are not aware of any other flight spectrometer that covers the broad solar reflectance and thermal emission spectral range with the spectral resolution needed to achieve the science goals discussed above. Moreover, MLPS is a relatively low mass and power instrument suitable for small spacecraft reconnaissance of asteroids, the Moon, and planetary satellites as well as mass-constrained landed missions.

The instrument design is shown in Fig. 2(a) with a complete ray trace. The instrument consists of a 2-mirror telescope, 3-mirror Offner-type relay with a diffraction grating at the secondary mirror position, a focal plane assembly (FPA) with two detector technologies, and a small cryocooler, all of which are mounted, for testing purposes, on an aluminum testbed bench sitting in a vacuum chamber (not shown here for clarity). The testbed bench is liquid cooled through a feedthrough connecting to an external benchtop chiller. The collimated beam enters a ZnSe window into the vacuum chamber and is focused by the telescope before entering into the Offner spectrometer. The beam is split into two diffracted beams by the bi-faceted grating, as illustrated by the colored rays in Fig. 2(a), and the two dispersed beams are then focused onto the barrier infrared detector (BIRD) and the thermopile, as shown in the inset in Fig. 2(a) and described further in Section 4.1. A lid on the focal plane housing with only two slits and order sorting filters blocks unwanted radiance.

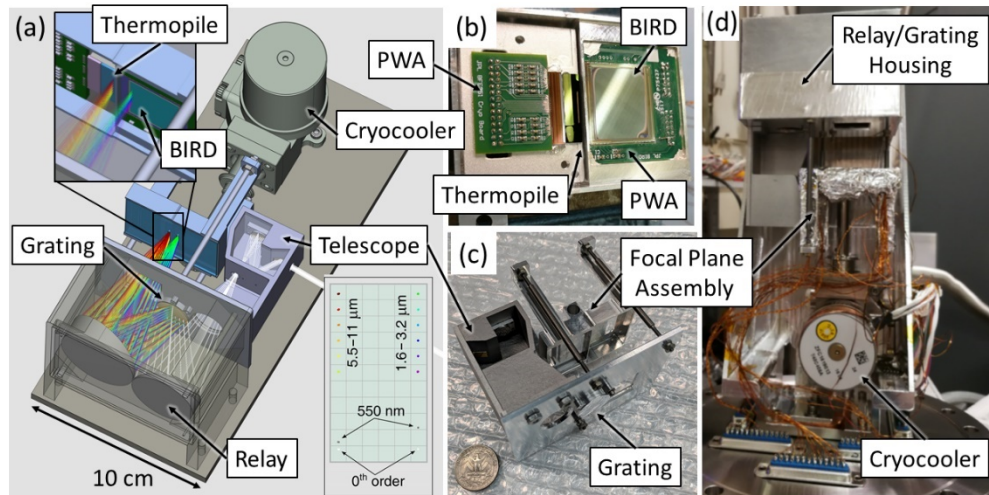


Fig. 2. The MLPS instrument. (a) The CAD model of the prototype with optical ray trace of the telescope and spectrometer (relay + grating) on the testbed bench, which fits in a custom small vacuum chamber. Both the cryocooler and spectrometer housing are mounted on the testbed bench. The telescope and FPA are mounted and aligned to the spectrometer housing. The testbed bench is cooled with circulating liquid to simulate the space environment. The top inset shows two columns of beams from the grating focused on the dual-sensor FPA, shown with the FPA lid removed. The ray colors illustrate spectral dispersion. The bottom inset shows the spectral map of the two beams at the image plane from ray trace simulation (grid size is 1 mm). The 2–4 μm band uses a BIRD and the 5.5–11 μm band uses a thermopile detector. (b) The dual FPA has the BIRD and the thermopile detectors mounted side-by-side with a distance of 5 mm, keeping the overall size of MLPS' optical assembly small. (c) The assembled FPA, telescope module, and grating on the mounting plate. (d) The fully assembled MLPS within its testbed, which is sitting on a vacuum flange. All signal wires from the FPA are connected to the electrical feedthroughs on the flange. A cold plate is mounted on the back side of the testbed.

The focal plane assembly includes two separate focal plane housings, one for the BIRD and the other for the thermopile. The BIRD architecture was developed to be the new generation of high-performance, cost-effective infrared detectors. The mid-wave infrared version used in MLPS is based on the InAs/InAsSb nBn material structure. The long wavelength cut-off can be tailored for the specific application. In Fig. 2(b), the BIRD and a printed wire assembly (PWA) are mounted on the right side of the focal plane assembly. On the left side, the thermopile, readout integrated circuit (ROIC) (Black Forest Engineering LLC version BFE384), and a PWA

are mounted on an aluminum plate, which is thermally isolated from the frame of the focal plane assembly. Each detector is thus thermally controlled separately as described in Section 4.2. The assembled hardware is shown in Figs. 2(b), (c) and (d). The overall dimensions of MLPS are $\sim 10 \text{ cm} \times 10 \text{ cm} \times 20 \text{ cm}$, which is 2U in volume.

MLPS is built upon three key technologies: a bi-faceted grating [15], a BIRD [16,17], and a thermopile detector [18–21] as shown in Fig. 3. We have customized and extended these technologies specifically for this instrument to make it possible to measure the MIR and LIR simultaneously in a payload that fits in a 2U volume. The bi-faceted diffraction grating disperses the input light into two parallel passbands of MIR (2–4 μm) and LIR (5.5–11 μm), with a spatial separation of 5 mm, as shown in Fig. 2(a). The detailed attributes of the instrument are summarized in Table 2. The Size, Weight, and Power (SWaP) stated in Table 2 are the current best estimate values based on the most likely configuration in which MLPS would fly. A BIRD integrated into a Santa Barbara Focalplane 193 ROIC is shown in Fig. 3(b). The BIRD is a 512×640 -pixel focal plane array (FPA) with 24 μm pitch. Because MLPS is a point spectrometer it uses only a single line of 200 pixels [see bottom inset in Fig. 2(a)], dispersed with a spectral resolution of 10 nm. Future iterations may consider imaging spectroscopy capabilities. The BIRD used in this work has a long wavelength cutoff of $\sim 5 \mu\text{m}$. Since MPLS is designed with a 4 μm cutoff, future iterations would use a chip tailored with a shorter cutoff wavelength to prevent unnecessary thermal noise [22]. The designed thermopile detector for MLPS has a line of 32 pixels with 225 μm pitch where only 22 pixels are used to cover the designed spectral range of 5.5–11 μm and to achieve a spectral resolution of 290 nm. The details of the thermopile are described in Refs. [18–21].

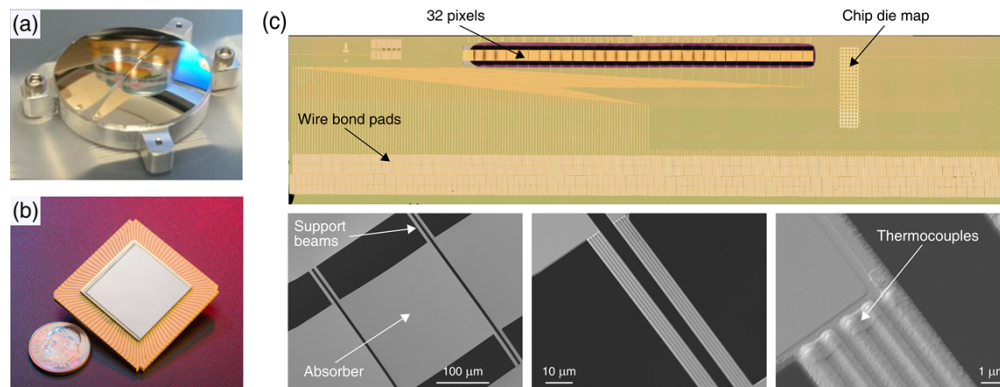


Fig. 3. Three key technologies from JPL are used in MLPS. (a) The bi-faceted grating. (b) A BIRD bonded to an SBF 193 ROIC sitting on a chip carrier. (c) A 32-pixel thermopile array and SEM images of the array

Table 2. MLPS instrument attributes

Attribute	Value	
CBE Volume	10 × 10 × 20 cm ³	
CBE Payload Mass	2.1 kg	
CBE Payload Power	7 W	
	MIR	LIR
Detector type	BIRD	Thermopile
Spectral coverage	2–4 μm	5.5–11 μm
FOV	3.0 mrad	27 mrad
F/#	2.3	
Focal length	8.2 mm	
Number of channels	200	22
Δλ	10 nm	290 nm
Pitch	24 μm	225 μm

3. Performance models

The spectral radiant power, measured in watts (W), reaching the MIR channel of MLPS is given by the following expression

$$\Phi_{\lambda} = \eta_o \eta_{g, \lambda} \tau_{sf, \lambda} L_{\lambda} \Delta \lambda A_i \Omega_{fsd} \left(\tau_{ZnSe, \lambda} / n^2 \right), \quad (1)$$

where

η_o — the efficiency of all the optics including the splitting efficiency (0.5) of the grating,

$\eta_{g, \lambda}$ — the efficiency of the grating,

$\tau_{sf, \lambda}$ — the transmission of the sorting filter in front of detectors,

L_{λ} — the incident spectral radiance of the source,

$\Delta \lambda$ — spectral resolution, see Table 2,

A_i — the image area projected on the detector, see Table 2,

Ω_{fsd} — the projected solid angle subtended at the detector,

$\tau_{ZnSe, \lambda}$ — the transmission of the ZnSe window,

n — the refractive index of air.

The terms in parentheses are specific to the laboratory test setup and are not applicable for the flight instrument. For laboratory sources, the spectral radiance L_{λ} is defined by Planck's equation for blackbody radiation expressed in term of wavelength [23]. In flight, the sun and planetary surface thermal emission are spectral radiance sources. The projected solid angle $\Omega_{fsd} = \pi/[4(f/\#)^2]$ is calculated according to the $f/\#$. The designed value of $f/\#$ is 2.3 as shown in Table 2.

3.1. MIR performance

With the spectral radiant power in Eq. (1), we can calculate the number of photons reaching each pixel of the BIRD array and then convert these photons into electrons (e.g., the signal in the MIR channel),

$$S_{MW,\lambda} = \frac{\Phi_{MW,\lambda} t_{int} Q}{hc/\lambda}, \quad (2)$$

where $\Phi_{MW,\lambda}$ is the spectral radiant power in the MIR channel, t_{int} is the integration time, hc/λ is the photon energy, and Q is the quantum efficiency. The noise in electron number is given by

$$n_{MW,\lambda} = \sqrt{(n_{read})^2 + (n_{dark})^2 + (n_{digit})^2 + (n_{photon})^2}, \quad (3)$$

where n_{read} is the read noise, n_{dark} is the dark current noise, n_{digit} is the digitization noise, and n_{photon} is the photon shot-noise and equals $\sqrt{S_{MW,\lambda}}$.

By combing Eq. (2) and (3), we get the SNR for the MIR channel as

$$SNR_{MW,\lambda} = \frac{S_{MW,\lambda}}{n_{MW,\lambda}} = \frac{S_{MW,\lambda}}{\sqrt{(n_{read})^2 + (n_{dark})^2 + (n_{digit})^2 + S_{MW,\lambda}}}. \quad (4)$$

3.2. LIR performance

The signal generated in a given thermopile detector in volts is expressed as,

$$S_{LW,\lambda} = \alpha_{gb} \Phi_{LW,\lambda} R_V, \quad (5)$$

where $\Phi_{LW,\lambda}$ is the spectral radiant power in the LIR channel, calculated according to Eq. (1). The value R_V is the voltage responsivity with the value of approximately 3600 V/W, and α_{gb} the absorption coefficient of the gold black optical coating on top of the absorber, which is nearly unity between 1 μm and 50 μm .

For the thermopile detectors discussed here the noise comes from two sources: Johnson noise and readout integrated circuit (ROIC) noise. (The 1/f noise and the temperature fluctuation noise are negligible [18].) The total noise in a given pixel in the LIR channel can be expressed in volts as the following,

$$n_{LW,\lambda} = \frac{\sqrt{4k_B T R + (n_{ROIC})^2}}{\sqrt{t_{int}}}, \quad (6)$$

where k_B is the Boltzmann constant, T the temperature of thermopile, $R = 100 \text{ k}\Omega$, the electrical resistance of the element, and $n_{ROIC} \approx 60 \text{ nV}/\sqrt{\text{Hz}}$, the readout circuit noise.

The SNR for the LIR channel is

$$SNR_{LW,\lambda} = \frac{S_{LW,\lambda}}{n_{LW,\lambda}} = \frac{S_{LW,\lambda} \sqrt{t_{int}}}{\sqrt{4k_B T R + (n_{ROIC})^2}}. \quad (7)$$

3.3. MLPS design performance modeling

The simulated SNR for the MIR channels of MLPS based on the above equations is shown in Fig. 4(a) and Fig. 4(b) assuming an airless target 1 AU (e.g. NEOs or the Moon) and 3 AU (e.g. main belt asteroids) from the sun, respectively, a surface albedo of 5%, and a solar incident angle to the surface of the target of 0 and 70 degrees for the 275 K and 200 K surface temperature case, respectively. For the MIR, the source of the spectral reflectance (see Eq. (1)) is dominated by reflected sunlight below about 2.8 μm , while thermal emission from the body contributes at longer wavelengths. In Fig. 4(c), the simulated SNR for the LIR channel is shown for the 1

1 AU and 3 AU cases of surface thermal emission. An integration time of 140 ms is assumed for Fig. 4(a), 1.1 s for Fig. 4(b), and 1.1 s for Fig. 4(c). (The ratio of the LIR to MIR integration time for the 1 AU case is equal to the ratio of the LIR to MIR IFOV shown in Table 2.)

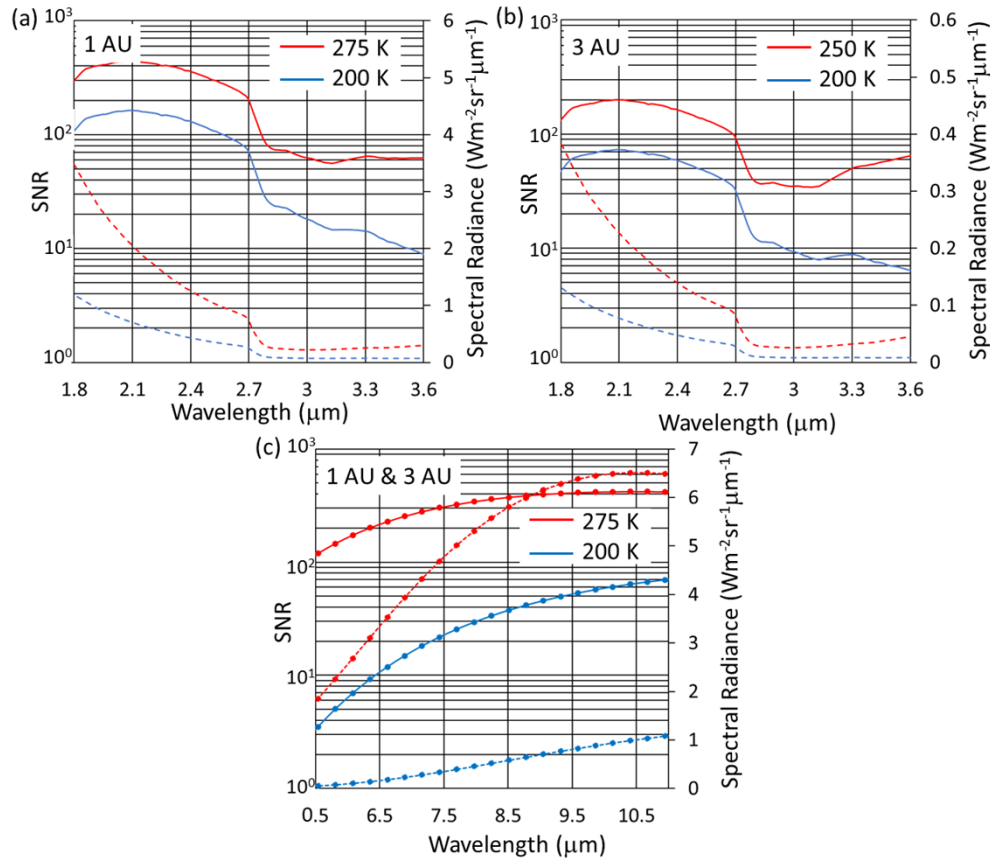


Fig. 4. The modeled performance of the designed instrument looking at an airless target (see text). (a) SNR (solid line) and spectral radiance (dashed line) of the MIR channel from a 1 AU target at 275 K and 200 K, (b) the MIR channel from a 3 AU target at 275 K and 200 K, and (c) the LIR channel from a blackbody 1 AU or 2 AU at 275 K and 200 K.

4. Implementation

MLPS is designed for space-borne applications and, therefore, the overall design and implementation of the prototype instrument incorporates proven design principles and components from previous instruments that have flown in space to minimize the risk of MLPS failing during flight. For the components of MLPS that have no heritage to previous flight instruments, optical testing of the prototype MLPS instrument validated these components' design and performance (see Section 4.3). A block diagram of a flight version of MLPS is shown in Fig. 5. The only distinction between the flight and laboratory version of MLPS shown in Fig. 2 is the inclusion of bipods to hold the MLPS payload, a radiator to reject heat mainly from the cryocooler, and the payload integrated electronics (PIE) which interface MLPS with the spacecraft. MLPS shares design heritage with NASA's Hyperspectral Thermal Imager (HyTI) and Polar Radiant Energy in the Far-Infrared Experiment (PREFIRE) as indicated in Fig. 5.

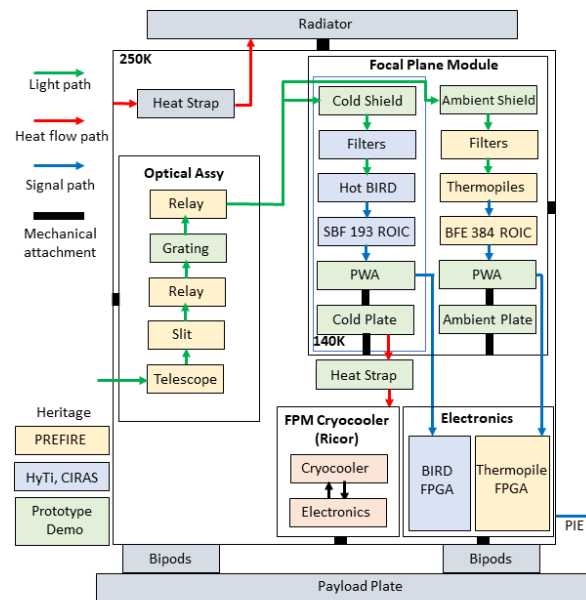


Fig. 5. Block diagram of MLPS. All the subsystems of MLPS have either flight heritage or have been demonstrated under flight-like conditions and shown to agree with the instrument model discussed in Section 3.

4.1. Optical design and performance

MLPS is an all-reflective design. This is required for a spectrometer that covers such a broad spectral passband because it eliminates any possibility of chromatic artifacts. The design combines a 2-mirror telescope with a 3-mirror Offner-type [24] spectrometer relay. All optical mirrors are diamond turned aluminum substrates and overcoated with gold using evaporative deposition. A pinhole is placed at the focus of the telescope which forms the instantaneous field of view (IFOV). A diffraction grating is placed at the secondary mirror position of the relay and forms the pupil stop for the overall system. MLPS uses a novel bi-faceted mirror substrate with a different diffraction grating written on each facet. The convex reflective bi-faceted grating is patterned by analog direct-write electron-beam (E-beam) lithography in PMMA resist on a convex diamond-turned substrate [15,25–27]. A standard blaze grating design as shown in Fig. 3(a) is used because each passband is a single octave.

Splitting the pupil and writing two different diffraction gratings on one substrate has the effect of combining two spectrometers into one. Precision tilts are written into the aluminum substrate to make sure each dispersion is held side by side. The two dispersions are held as close together as possible while still maintaining acceptable optical aberrations. A distance of 5 mm separation at the focal plane is consistent with the minimum distance possible between the two detector arrays, BIRD and thermopile. Unique focal plane packaging is necessary to realize the 5 mm separation and to keep the overall size of MLPS small. To the best of our knowledge, this is the first time that two different diffraction grating designs have been fabricated by E-beam lithography on a bi-faceted convex substrate, which is fundamental to making MLPS a dual wavelength range, broadband spectrometer with high spectral resolution in a small volume.

The Offner relay is shown in the MLPS configuration in Fig. 2(a). The figure shows both the conceptual model and actual system. The Offner stop is located at the position of the secondary mirror and the entrance and exit pupils are at infinity. All odd aberrations are theoretically cancelled out since the Offner design in its pure form is symmetric about the stop. The bi-faceted

grating breaks the symmetry, so the grating tilt is allowed to vary in the design to counter balance the effects. ZEMAX (Zemax LLC, Kirkland, Washington) is used for all merit function creation and design optimization. The main goal was to find a design which balances astigmatism for a 2-D field stop while maintaining an acceptable object space numerical aperture (NA). Our MLPS Offner optical system has the primary mirror split into a primary and tertiary to minimize the size and allow aberration optimization between the two mirrors.

4.2. Thermal design and performance

The thermal management includes active cooling of different zones of the MLPS instrument to different set temperatures. The BIRD and the thermopile detectors require different thermal environments for the desired signal-to-noise performance. This is done while maintaining them at close physical proximity due to the shared light path. The spectrometer also must be kept at low temperature to minimize thermal load on the BIRD.

Figure 6. shows the thermal diagram of MLPS integrated into the testbed with temperatures for the different components indicated and the heat flow between them. The aluminum FPA is mounted to the spectrometer housing with 31/8-inch diameter by 1.5-inch long Ti6Al4V rods to reduce the thermal load on the FPA as shown in Fig. 2. The FPA housing is wrapped with multi-layer insulation (MLI) sheets to reduce the emissivity, which in turn reduces the radiative absorption from the inside wall of the vacuum chamber. The BIRD chip and the PWA are thermally coupled to the FPA housing while the thermopile and its ROIC and PWA are thermally isolated. The thermopile chip, ROIC and PWA are mounted on an aluminum plate, which is mounted to the FPA housing by three low thermal conductivity ceramic rods to isolate the thermopile chip from the FPA housing. A heater is mounted on the backside of this aluminum plate and another PID controller controls the temperature to 200 K.

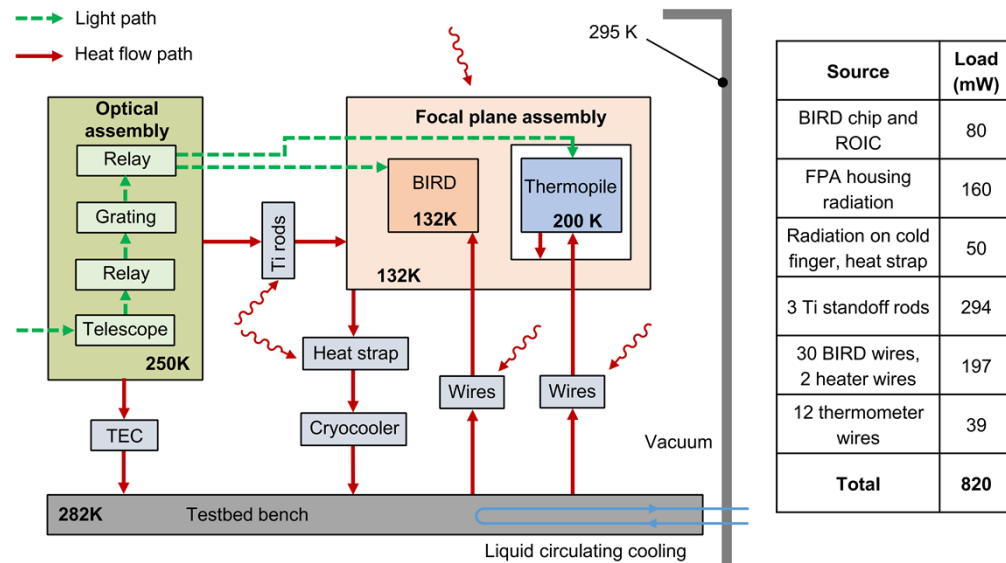


Fig. 6. Thermal management diagram of the testbed. The surroundings correspond to the inside wall of the vacuum chamber, which is 295 K. The cold finger temperature of the cryocooler, the FPA, and the thermopile are PID controlled separately. The optical assembly is cooled by a thermoelectric module. The table shows the calculated heat flow between the various components of the FPA and cryocooler.

The testbed bench as shown in Figs. 2(a) and 2(d) is maintained at 282 K by a cold plate with circulating polycool EG -25 coolant that serves as a heat sink for the cryocooler. The optical

assembly including the spectrometer, telescope and all the optics inside as shown in Figs. 2(a) and 2(d) are cooled down from 282 K to 250 K by thermoelectric cooling modules. For the flight version, the heat sink of the cryocooler and optics will be cooled via a radiator to space as shown in Fig. 5.

A Ricor K508N rotary Stirling cryocooler [28,29], charged with 30 bar helium and running at 23 Vdc, provides the cooling for the FPA. A thermal strap connects the FPA and the cold finger of the cooler. The closed-loop mode is applied to run the cryocooler, which keeps the cold finger within ± 5 mK stability at a temperature slightly lower than the desired FPA temperature with the internal PID controller in the cooler. A heater on the FPA and an external PID controller together maintain the FPA housing and the BIRD at 132 K within ± 2 mK stability.

Using the Ross plot in Fig. 7, we built a thermal model for MLPS. The model is based on the thermal environment in the test chamber, including the temperature, emissivity, and geometry of each component, and the results are summarized in the table in Fig. 6. The thermal loads are mainly from the power consumption in the BIRD, the FPA housing radiative absorption, the conduction from standoff rods, signal wires, and the thermometer and heater wires, of which the largest contribution comes from the standoff rods. The second largest load comes from the signal and heater wires. For each of these wires, one end is thermally anchored to the FPA housing or the thermally isolated thermopile plate, and the other end is thermally anchored to the testbed bench at 282 K.

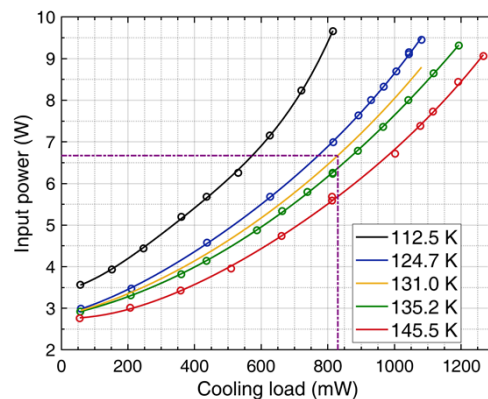


Fig. 7. Ross plot of Ricor K508N. The cooler runs in vacuum where it is mounted to a bench with a temperature between 290 K and 295 K. The circles are measured points, and solid curves are fitted. The curve for 131 K is interpolated between the neighboring curves. The dashed-dotted purple line indicates the cooling power at 131 K with a known input power.

A thermal balance test is done by comparing the thermal loads calculated from the thermal model above with the predictions from the performance curves of the cryocooler. The total thermal load on the cryocooler cold finger can be estimated from the Ross plot of thermal performance of cryocooler K508N when running in closed-loop [29], as shown in Fig. 7. When the input power of the cryocooler running at a specific cold finger temperature is known, the cooling power can be found correspondingly on the Ross plot. For example, for an input power of 6.6 W, the cooling power is estimated to be ~ 830 mW which agrees with the model in the table in Fig. 6.

4.3. System performance with laboratory blackbody source

In the laboratory demonstration, a blackbody source at different temperatures is used to measure the spectral response of MLPS while MLPS is under vacuum and thermally controlled as shown in Fig. 6. To test MLPS's performance, a pinhole with a diameter of 500 μm is placed at the

focus of the telescope which forms the instantaneous field-of-view (IFOV). Together with an off-axis parabolic (OAP) mirror, the blackbody source becomes a collimated source entering the ZnSe window. The OAP stops down the aperture of MLPS which in turns limits the etendue. Due to resource limitations, an optimal setup was not established for this measurement, but the difference in effective $f/\#$ was deemed minor with modifications to the source compensating for the signal deficient from a traditional scene.

Due to photons reaching the BIRD from room temperature sources, such as the ZnSe window, the OAP, the pinhole, and the walls of the vacuum chamber, a long integration time on the MIR detector is limited to avoid saturation. Consequently, in the test setup, high temperatures from the blackbody source at 2 ms integration are used to excite the BIRD directly, rather than a reflected signal as shown in Fig. 4(a). Moreover, the use of the OAP reduces the etendue one would see in flight, making it necessary to increase the temperature of the blackbody over the values shown in Fig. 4.

The SNR from the ratio of the measured signal and noise and the radiometric model predictions at different temperatures from 600 K to 740 K in the MIR channel are shown in Fig. 8(a). The radiometric model predictions match the measurement well in the working spectral range, indicating the BIRD array and optics are behaving as expected. For the flight version, the BIRD cut-off wavelength will be at 4 μm , and there will be no room temperature environment, the background count is expected to be reduced significantly, enabling much longer integration.

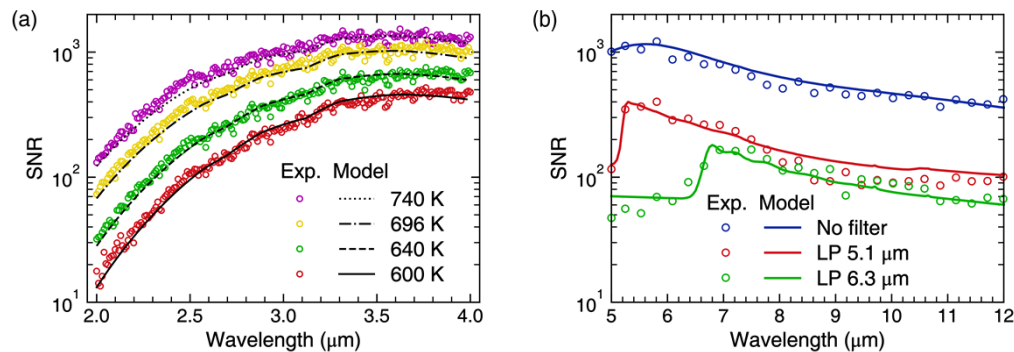


Fig. 8. Demonstration of the ratio of measured spectral response to measured noise (SNR) (open circles) relative to model prediction (lines). (a) The MIR channel SNR from measurements (see Eq. (4)) and model is shown for 4 different blackbody temperatures with an integration time of 2 ms. The black lines show the MLPS model while measurements obtained are shown with open circles. (b) The LIR channel SNR at 1000 K with and without longwave filters, with cutoff wavelength at 5.1 μm and 6.3 μm , respectively.

For the LIR channels, a measurement taken at 1000 K is shown in Fig. 8(b). The radiometric model prediction also matches the measurement both with or without longwave filters. We note again that the experimental setup with the OAP and pin hole reduce the etendue of the system compared to the flight configuration so the temperature of the blackbody is higher than that shown in Fig. 4(c). Importantly, the spectral response of MLPS agrees with the model in the benchtop configuration; therefore, under flight the conditions, MLPS will achieve the performance shown in Fig. 4.

5. Conclusions

A miniature, dual-wavelength range point spectrometer, MLPS, has been built and demonstrated at the mid-wave infrared (2–4 μm) and long-wave infrared (5.5–11 μm) ranges. MPLS enables comprehensive compositional, mineralogic, and thermophysical science from a single data set.

The prototype instrument requires little resources with a mass of ~ 2 kg, a volume of $10\text{ cm} \times 10\text{ cm} \times 20\text{ cm}$, and a power consumption of $< 10\text{ W}$ so it is particularly well-suited for small satellite and landers. The demonstrated SNR matches the radiometric models and satisfies the design requirements for analyzing quantitative compositional and thermal information from reflected and emitted light from a wide range of a surfaces. MLPS is at a technology readiness level of 6, making it ready to be proposed to near-term opportunities.

Funding. Jet Propulsion Laboratory; National Aeronautics and Space Administration.

Acknowledgments. The authors thank Dean Johnson of JPL for providing Ricor cryocooler information; Sir (Don) B. Rafol of JPL for providing characteristic data of BIRD; Byeong H. Eom of JPL for valuable comments and discussions on thermopile ROIC characterization.

Disclosures. The authors declare no conflicts of interest.

Data availability. Data underlying the results presented in this paper are not publicly available at this time but may be obtained from the authors upon reasonable request.

References

1. M. C. De Sanctis, A. Coradini, E. Ammannito, G. Filacchione, M. T. Capria, S. Fonte, G. Magni, A. Barbis, A. Bini, M. Dami, I. Ficai-Veltroni, G. Preti, and V. I. R. Team, "The VIR Spectrometer," *Space Sci. Rev.* **163**(1-4), 329–369 (2011).
2. T. Okada, T. Fukuhara, S. Tanaka, M. Taguchi, T. Imamura, T. Arai, H. Senshu, Y. Ogawa, H. Demura, K. Kitazato, R. Nakamura, T. Kouyama, T. Sekiguchi, S. Hasegawa, T. Matsunaga, T. Wada, J. Takita, N. Sakatani, Y. Horikawa, K. Endo, J. Helbert, T. G. Müller, and A. Hagermann, "Thermal Infrared Imaging Experiments of C-Type Asteroid 162173 Ryugu on Hayabusa2," *Space Sci. Rev.* **208**(1-4), 255–286 (2017).
3. P. R. Christensen, V. E. Hamilton, G. L. Mehall, D. Pelham, W. O'Donnell, S. Anwar, H. Bowles, S. Chase, J. Fahlgren, Z. Farkas, T. Fisher, O. James, I. Kubik, I. Lazbin, M. Miner, M. Rassas, L. Schulze, K. Shamordola, T. Tourville, G. West, R. Woodward, and D. Lauretta, "The OSIRIS-REx Thermal Emission Spectrometer (OTES) Instrument," *Space Sci. Rev.* **214**(5), 87 (2018).
4. E. B. Johnson, C. Hardgrove, R. Starr, S. Vogel, R. Frank, G. Stoddard, S. West, and J. Christian, "Development of the LunaH-Map miniature neutron spectrometer," *Proc. SPIE* **10392**, 103920H (2017).
5. D. Daou, "Small innovative missions for planetary exploration," in *European Planetary Science Congress 2017* (Abstract #EPSC2017-146, 2007).
6. P. Voosen, "NASA to pay private space companies for moon rides," *Science* **362**(6417), 875–876 (2018).
7. M. D. Dyar, C. A. Hibbits, and T. M. Orlando, "Mechanisms for incorporation of hydrogen in and on terrestrial planetary surfaces," *Icarus* **208**(1), 425–437 (2010).
8. D. Takir and J. P. Emery, "Outer Main Belt asteroids: Identification and distribution of four 3- μm spectral groups," *Icarus* **219**(2), 641–654 (2012).
9. C. M. Pieters, J. N. Goswami, R. N. Clark, M. Annadurai, J. Boardman, B. Buratti, J.-P. Combe, M. D. Dyar, R. Green, J. W. Head, C. Hibbits, M. Hicks, P. Isaacson, R. Klima, G. Kramer, S. Kumar, E. Livo, S. Lundeen, E. Malaret, T. McCord, J. Mustard, J. Nettles, N. Petro, C. Runyon, M. Staid, J. Sunshine, L. A. Taylor, S. Tompkins, and P. Varanasi, "Character and spatial distribution of OH/H₂O on the surface of the Moon seen by M3 on Chandrayaan-1," *Science* **326**(5952), 568–572 (2009).
10. K. K. Materese, D. P. Cruikshank, S. A. Sandford, H. Imanaka, and M. Nuevo, "Ice chemistry on outer solar system bodies: electron radiolysis of N₂-, CH₄-, and CO-containing ices," *Astrophys. J.* **812**(2), 150 (2015).
11. M. M. McAdam, J. M. Sunshine, K. T. Howard, and T. M. McCoy, "Aqueous alteration on asteroids: Linking the mineralogy and spectroscopy of CM and CI chondrites," *Icarus* **245**, 320–332 (2015).
12. T. D. Glotch, P. G. Lucey, J. L. Bandfield, B. T. Greenhagen, I. R. Thomas, R. C. Elphic, N. Bowles, M. B. Wyatt, C. C. Allen, K. D. Hanna, and D. A. Paige, "Highly Silicic Compositions on the Moon," *Science* **329**(5998), 1510–1513 (2010).
13. A. D. Rogers, N. H. Warner, M. P. Golombek, J. W. Head, and J. C. Cowart, "Areal Extensive Surface Bedrock Exposures on Mars: Many Are Clastic Rocks, Not Lavas," *Geophys. Res. Lett.* **45**(4), 1767–1777 (2018).
14. M. C. De Sanctis, A. Raponi, E. Ammannito, M. Ciarniello, M. J. Toplis, H. Y. McSween, J. C. Castillo-Rogez, B. L. Ehlmann, F. G. Carozzo, S. Marchi, F. Tosi, F. Zambon, F. Capaccioni, M. T. Capria, S. Fonte, M. Formisano, A. Frigeri, M. Giardino, A. Longobardo, G. Magni, E. Palomba, L. A. McFadden, C. M. Pieters, R. Jaumann, P. Schenk, R. Mugnuolo, C. A. Raymond, and C. T. Russell, "Bright carbonate deposits as evidence of aqueous alteration on (1) Ceres," *Nature* **536**(7614), 54–57 (2016).
15. D. W. Wilson, P. D. Maker, R. E. Muller, P. Z. Mouroulis, and J. Backlund, "Recent advances in blazed grating fabrication by electron-beam lithography," *Proc. SPIE* **5173**, 51730E (2003).
16. D. Z.-Y. Ting, C. J. Hill, A. Soibel, S. A. Keo, J. M. Mumolo, J. Nguyen, and S. D. Gunapala, "A high-performance long wavelength superlattice complementary barrier infrared detector," *Appl. Phys. Lett.* **95**(2), 023508 (2009).

17. D. Z.-Y. Ting, A. Soibel, A. Khoshakhlagh, J. Nguyen, L. Höglund, S. A. Keo, J. M. Mumolo, and S. D. Gunapala, "Exclusion, extraction, and junction placement effects in the complementary barrier infrared detector," *Appl. Phys. Lett.* **102**(12), 121109 (2013).
18. M. C. Foote, E. W. Jones, and T. Caillat, "Uncooled thermopile infrared detector linear arrays with detectivity greater than 10^9 cmHz^{1/2}/W," in *IEEE Transactions on Electron Devices* (IEEE, 1998), **45**, pp. 1896–1902.
19. M. C. Foote, M. Kenyon, T. R. Krueger, T. A. McCann, R. Chacon, E. W. Jones, M. R. Dickie, J. T. Schofield, D. J. McCleese, S. Gaalema, and W. Hu, "Thermopile detector arrays for space science applications," in *International Workshop on Thermal Detectors for Space Based Planetary, Solar, and Earth Science Applications* (TDW, 2003), p. 5.
20. M. C. Foote and E. W. Jones, "High-performance micromachined thermopile linear arrays," *Proc. SPIE* **3379**, 192–197 (1998).
21. G. Mariani and M. Kenyon, "Room-temperature remote sensing: Far-infrared imaging based on thermopile technology," in *2015 40th International Conference on Infrared, Millimeter, and Terahertz Waves (IRMMW-THz)* (2015), pp. 1–2.
22. A. Soibel, D. Z. Ting, C. J. Hill, A. M. Fisher, L. Hoglund, S. A. Keo, and S. D. Gunapala, "Mid-wavelength infrared InAsSb/InSb nBn detector with extended cut-off wavelength," *Appl. Phys. Lett.* **109**(10), 103505 (2016).
23. David G Andrews, *An Introduction to Atmospheric Physics* (Cambridge University Press, 2010).
24. A. Offner, "Unit power imaging catoptric anastigmat," United States patent US 3,748,015 (July 24, 1973).
25. P. Maker, R. Muller, D. Wilson, and P. Mouroulis, "New Convex Grating Types Manufactured by Electron Beam Lithography," in *Diffractive Optics and Micro-Optics 10*, OSA Technical Digest Series (1998), pp. 234–236.
26. P. Mouroulis, D. W. Wilson, P. D. Maker, and R. E. Muller, "Convex grating types for concentric imaging spectrometers," *Appl. Opt.* **37**(31), 7200–7208 (1998).
27. P. D. Maker, R. E. Muller, and D. W. Wilson, "Diffractive optical elements on non-flat substrates using electron beam lithography," United States patent US 6,480,333 B1 (November 12, 2002).
28. D. L. Johnson, M. J. Lysek, and J. M. Morookian, "The Ricor K508 cryocooler operational experience on Mars," *AIP Conf. Proc.* **1573**(1), 1792–1799 (2014).
29. M. A. Mok, I. M. McKinley, and A. J. Mastropietro, "Thermal and exported vibration characterization of RICOR K508N cryocooler," *IOP Conf. Ser.: Mater. Sci. Eng.* **755**(1), 012010 (2020).